nanomaterials

MDPI

Article

Magnetic-Core–Shell–Satellite Fe_3O_4-Au@Ag@(Au@Ag) Nanocomposites for Determination of Trace Bisphenol A Based on Surface-Enhanced Resonance Raman Scattering (SERRS)

Jie Huang [1], Tianxiang Zhou [1], Wenshi Zhao [1,2], Min Zhang [1], Zhibo Zhang [1], Wangsheng Lai [1], Naveen Reddy Kadasala [3], Huilian Liu [1,*] and Yang Liu [1,*]

[1] Key Laboratory of Functional Materials Physics and Chemistry of the Ministry of Education, Jilin Normal University, Changchun 130103, China
[2] Changchun Institute of Optics, Fine Mechanics and Physics, Chinese Academy of Sciences, Changchun 130033, China
[3] Department of Chemistry, Towson University, Towson, MD 21252, USA
* Correspondence: lhl541@126.com (H.L.); liuyang@jlnu.edu.cn (Y.L.)

Abstract: As a typical representative of endocrine-disrupting chemicals (EDCs), bisphenol A (BPA) is a common persistent organic pollutant in the environment that can induce various diseases even at low concentrations. Herein, the magnetic Fe_3O_4-Au@Ag@(Au@Ag) nanocomposites (CSSN NCs) have been prepared by self-assembly method and applied for ultra-sensitive surface-enhanced resonance Raman scattering (SERRS) detection of BPA. A simple and rapid coupling reaction of Pauly's reagents and BPA not only solved the problem of poor affinity between BPA and noble metals, but also provided the SERRS activity of BPA azo products. The distribution of hot spots and the influence of incremental introduction of noble metals on the performance of SERRS were analyzed by a finite-difference time-domain (FDTD) algorithm. The abundance of hot spots generated by core–shell–satellite structure and outstanding SERRS performance of Au@Ag nanocrystals were responsible for excellent SERRS sensitivity of CSSN NCs in the results. The limit of detection (LOD) of CSSN NCs for BPA azo products was as low as 10^{-10} M. In addition, the saturation magnetization (Ms) value of CSSN NCs was 53.6 emu·g^{-1}, which could be rapidly enriched and collected under the condition of external magnetic field. These magnetic core–shell–satellite NCs provide inspiration idea for the tailored design of ultra-sensitive SERRS substrates, and thus exhibit limitless application prospects in terms of pollutant detection, environmental monitoring, and food safety.

Keywords: magnetic; core–shell–satellite nanocomposites; surface-enhanced resonance Raman scattering; coupling reaction; FDTD; bisphenol A

Citation: Huang, J.; Zhou, T.; Zhao, W.; Zhang, M.; Zhang, Z.; Lai, W.; Kadasala, N.R.; Liu, H.; Liu, Y. Magnetic-Core–Shell–Satellite Fe_3O_4-Au@Ag@(Au@Ag) Nanocomposites for Determination of Trace Bisphenol A Based on Surface-Enhanced Resonance Raman Scattering (SERRS). *Nanomaterials* **2022**, *12*, 3322. https://doi.org/10.3390/nano12193322

Academic Editor: Wen-Huei Chang

Received: 23 August 2022
Accepted: 21 September 2022
Published: 24 September 2022

1. Introduction

Endocrine-disrupting chemicals (EDCs), also known as environmental hormones, are exogenous substances that affect mammalian reproduction by interfering with the endocrine system of organisms [1–3]. Bisphenol A (BPA), as a typical representative of EDCs, has been used principally in manufacturing polycarbonates and epoxy resins which are the main raw materials of plasticizers, plastic bottles and cups, food storage and packaging materials, and other commonly used industrial products [4,5]. Unfortunately, a large amount of evidence shows that the persistence, bioaccumulation, and biomagnification of BPA can bring about serious negative effects on human health and the ecosystem [6,7]. Although BPA is a low-toxicity chemical, it can induce a variety of diseases even at very low concentrations, such as congenital disabilities, diabetes, cardiovascular diseases, multiple cancers, and especially reproductive system diseases [8–10]. Hence, it is urgent to explore a rapid, sensitive, efficient, and low-cost detection method for BPA.

At present, direct detection and indirect detection are two commonly used methods for BPA detection. The direct detection method of BPA mainly includes high-performance liquid chromatography (HPLC), gas chromatography/mass spectrometry (GC-MS) and liquid chromatography/mass spectrometry (LC-MS) [11–13]. Nevertheless, these methods ordinarily need complex sample pretreatment, long-term testing, professional testers, and expensive equipment, which limit their practical application. By comparison, indirect detection methods, such as plasmon resonance biosensors and enzyme-linked immunosorbent assay, have high sensitivity [14,15]. However, the complex antibody preparation and the blurry recognition boundaries between specificity and non-specificity still need to be solved [16]. In recent years, as a highly sensitive spectral analysis technology, surface-enhanced Raman scattering (SERS) has stimulated considerable research enthusiasm due to its high sensitivity, easy operation, multiplexing ability, and applicability, and it is extensively used in the detection of chemical and biological molecules [17–20]. Both electromagnetic enhancement (EM) and chemical enhancement (CE) are widely recognized SERS enhancement mechanisms [21,22]. A large number of experimental results have proven that the EM mechanism shows an enhancement of 10^4 to 10^{11}, while the CE mechanism only contributes to 10 to 10^3 enhancement [23]. Therefore, it is widely acknowledged that EM plays a key role in SERS enhancement [24]. Given that the enhancement of EM caused by localized surface plasmon resonance (LSPR) excitation usually occurs in nanogaps between metal nanoparticles (named "hot spots"), it is highly desirable to increase the number of "hot spots" for obtaining high performance SERS substrates [25–27].

Inducing aggregation and constructing interlayers are two commonly used methods for introducing high- density hot spots. Nonetheless, the introduction of aggregation will inevitably bring about non-uniform distribution of noble metals, which is not conducive to the purpose of increasing hot spots [28]. In comparison, the use of polymers to achieve the adsorption or self-assembly of hot spots on surface of composite SERS substrates has attracted more and more attention [29,30]. Polyethyleneimine dithiocarbamate (PEI-DTC) polymer with excellent bonding strength is an ideal interlayer, which can significantly improve the affinity of Au and Ag nanocrystals to the SERS surfaces due to the presence of the bidentate ligands with two chelating sulfur groups [31]. Unfortunately, single-element Au nanocrystals or Ag nanocrystals have limited plasmonic absorption [32]. The bimetallic Au@Ag nanocrystals can not only have richer plasmonic modes and tunable LSPR but also make full use of outstanding SERS activity of Ag nanocrystals as well as uniformity and stability of Au nanocrystals [33–35]. However, the affinity between phenolic molecules such as BPA and noble metals is rather weak when mixing the target analytes with noble metal substrates directly, which is bad for the acquisition of high-quality SERS signals [36]. Because azo dyes have a propensity to bind to noble metal nanocrystals, the coupling reaction of BPA and diazonium ions to produce azo dyes is an ideal solution for the SERS detection of BPA, which can greatly boost the activity of SERS substrates [37]. In addition, the resonance enhancement occurs when the excitation wavelength overlaps or approaches the electronic transition of target molecules, which is called surface-enhanced resonance Raman scattering (SERRS) [38]. Therefore, the combination of azo dyes derived from BPA and SERRS will make it possible for ultra-sensitive detection of BPA.

Herein, we propose magnetic-core–shell–satellite Fe_3O_4-Au@Ag@(Au@Ag) nanocomposites (CSSN NCs), which could serve as ultra-sensitive SERRS substrates for BPA detection. A simple and rapid coupling reaction of Pauly's reagents and BPA was used not only to solve the problem of poor affinity between BPA and noble metals, but also to advance SERRS enhancement performance. BPA azo products were selected as target molecules to discuss the effect of the incremental introduction of noble metals on SERRS activity. The distribution of hot spots was obtained by a finite-difference time-domain (FDTD) theoretical method, and the relevant SERRS enhancement mechanism was discussed. Given that Fe_3O_4 hollow spheres with large specific surface area have a good superparamagnetic property, CSSN NCs could be easily recovered through an external magnet, which provided potential possibilities of recycling and reuse in complex liquid environments [39]. Our work not

only enriches research on the tailored design of ultra-sensitive SERRS substrates, but also realizes the rapid and quantitative detection of trace BPA, which may have many possible applications, such as in pollutant detection, environmental monitoring, and food safety.

2. Materials and Methods

2.1. Materials and Characterization

The details of this section can be found in Supplementary Materials.

2.2. Synthesis of PEI-DTC Aqueous Solution, Fe_3O_4 Hollow Spheres, Au Seeds, and Au@Ag Nanocrystals

PEI-DTC aqueous solution, Fe_3O_4 hollow spheres, Au seeds, and Au@Ag nanocrystals were obtained on the basis of our previous work [40].

2.3. Synthesis of Fe_3O_4-Au (FA) NCs

An amount of 20 mg of Fe_3O_4 hollow spheres were added to 20 mL of methanol, followed by dropwise addition of 25 mL of PEI-DTC aqueous solution. After the mixture stood for 60 min, the product was separated and gathered by a magnet. Then 20 mL of Au seeds were added under sonication. Finally, FA NCs were obtained after continuous sonication for 1 h and repeated washing.

2.4. Synthesis of FA@Ag@(Au@Ag) (CSSN) NCs

As illustrated in Scheme 1, the preparation process of CSSN NCs consists of two steps. The first step was the preparation of FA@Ag NCs. First, 10 mg of FA NCs and 5 mL of deionized water were mixed. Subsequently, $AgNO_3$ (0.1 M; 3 mL) and reductant $NH_2OH{\cdot}HCl$ (0.1 M; 12 mL) were added. FA@Ag NCs were obtained after sonication for 2 h and several wash cycles with ethanol.

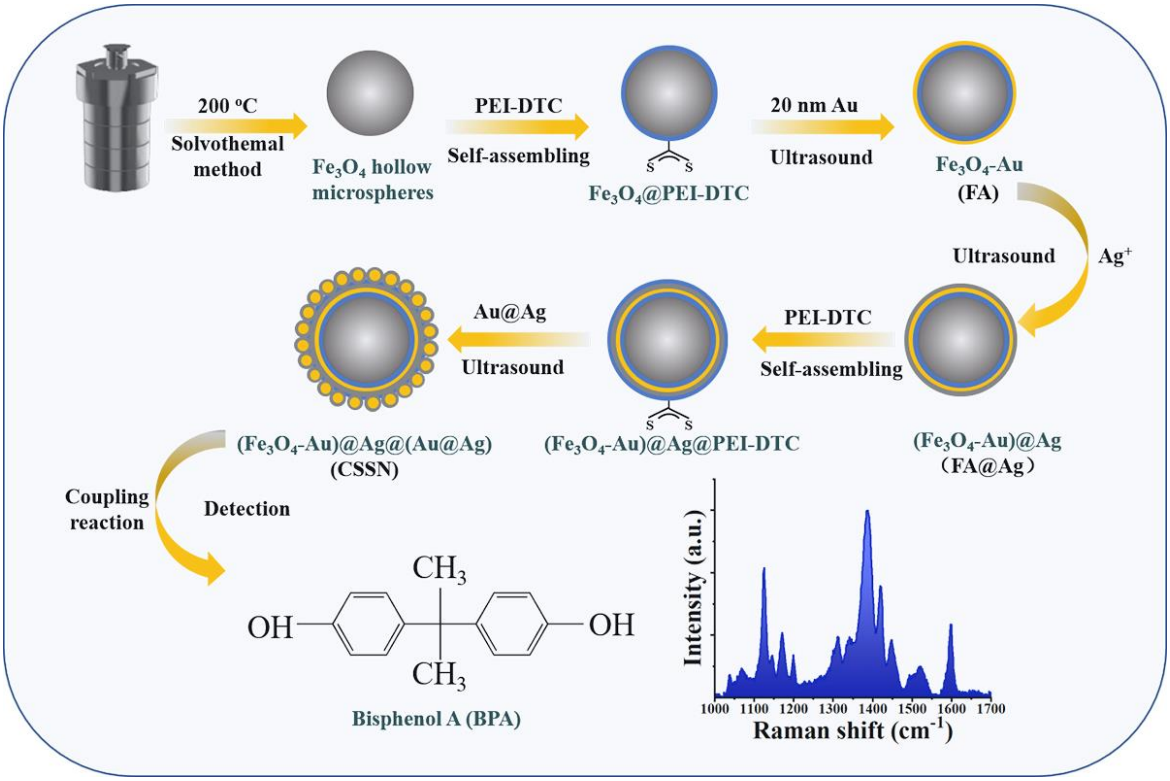

Scheme 1. Scheme of synthetic process of CSSN NCs and SERRS detection protocol for BPA on CSSN SERRS substrates.

The second step was the synthesis of CSSN NCs. The previously obtained FA@Ag NCs were blended with 20 mL of methanol, and 25 mL of PEI-DTC was dropwise-added. The mixture was stored for about 1 h. Then, FA@Ag@PEI-DTC NCs were obtained through washing and drying. After 10 mg of FA@Ag@PEI-DTC NCs was put into 5 mL of deionized water, 40 mL of Au@Ag nanocrystals was poured into the mixture and sonicated for about 2 h. Finally, the product was washed and dried to obtain CSSN NCs.

2.5. Pauly's Reagents and Coupling Reaction

Three kinds of reagents were prepared and kept at 4 °C for further use. Reagent A was a mixture of *p*-aminobenzenesulfonic acid (4.5 g), HCl solution (12 M; 5 mL) and deionized water (500 mL). Reagent B was 5% $NaNO_2$, and reagent C was 10% Na_2CO_3.

Coupling reaction: Reagents A + B + C + BPA ethanol solution in a volume ratio of 1:1:1:2.

2.6. FDTD Algorithm Method

Details of FDTD algorithm method can be found in Supplementary Materials.

2.7. SERRS Measurements

Before SERRS measurements, BPA was changed into azo dyes through a coupling reaction of BPA and diazonium ions to bind noble metals with high affinity and thus achieve highly sensitive detection of BPA. In this work, the phenol group of BPA could be converted into azo dyes with *p*-aminobenzenesulfonic acid through electrophilic aromatic substitution [41,42]. After the coupling reaction, BPA solution (25 μL) with different concentrations of 10^{-10} to 10^{-4} M and CSSN (1 mg) NCs were mixed in the aluminum pan, respectively. SERRS spectroscopy was performed under 514.5 nm laser and acquisition time was about 10 s.

3. Results and Discussion

3.1. Structure and Magnetic Properties of CSSN NCs

XRD technology was used to study the structure and phase purity of Fe_3O_4 hollow spheres, FA, FA@Ag and CSSN NCs. As shown in Figure 1, the diffraction peaks of Fe_3O_4 hollow spheres located at 30.4°, 35.5°, 43.4°, 53.4°, 57.3°, and 62.8° refer to the (112), (211), (220), (024), (303), and (224) planes of Fe_3O_4, respectively, which can be indexed to the cubic inverse spinel structure of Fe_3O_4 (JCPDS 19-0629) [43,44]. In addition, the diffraction peaks are sharp and strong, which indicates that the prepared Fe_3O_4 hollow spheres have high phase purity and good crystallization. However, owing to the fact that Fe_3O_4 as well as γ-Fe_2O_3 have the identical spinel structure, it is not sufficient to identify them only by XRD results [45]. Therefore, the phase structure of Fe_3O_4 hollow spheres was further verified by Mössbauer spectroscopy. As depicted in Figure S1, the Mössbauer spectrum of Fe_3O_4 hollow spheres can be fitted into two sextets, and the magnetic sextets lines illustrate the typical double six peak structure of Fe_3O_4 [46,47]. The corresponding Mössbauer parameters of Fe_3O_4 hollow spheres are presented in Table S1. Hyperfine field is 48.7 and 45.5 Tesla, and the isomer displacement is 0.288 and 0.602 mm/s, which correspond to Fe^{2+} and Fe^{3+} at octahedral interstitial sites and Fe^{3+} at tetrahedral interstitial sites. After Au seeds were loaded on surfaces of Fe_3O_4 hollow spheres, four new XRD diffraction peaks emerged at 38.2°, 44.3°, and 64.5°, which were assigned to (111), (200), and (220) planes of Au (JCPDS 04-0784) [48]. It should be noted that the positions of Au and Ag characteristic peaks are too close to be distinguished [49]. Since the intensities of XRD diffraction peaks are related to the contents of phase in the mixture [50,51], the increase of the intensities of Ag/Au diffraction peaks in the XRD patterns of FA@Ag NCs proves that there is dense Ag adsorbed on the surfaces of FA NCs. The XRD pattern of CSSN NCs shows that the diffraction peaks intensity of Ag/Au further increases significantly when the Au@Ag nanocrystals are adhered to the FA@Ag NCs. By contrast, the XRD diffraction pattern of CSSN NCs exhibits weaker Fe_3O_4 characteristic peaks than that of Fe_3O_4 hollow

spheres, FA, and FA@Ag NCs. This may be attributed to the declining proportion of Fe_3O_4 contents caused by the successful modification of the large amount of Au seeds and Au@Ag nanocrystals. Consequently, the information obtained from above XRD and Mössbauer analysis preliminary confirm the successful construction of Fe_3O_4 hollow spheres, FA, FA@Ag, and CSSN NCs.

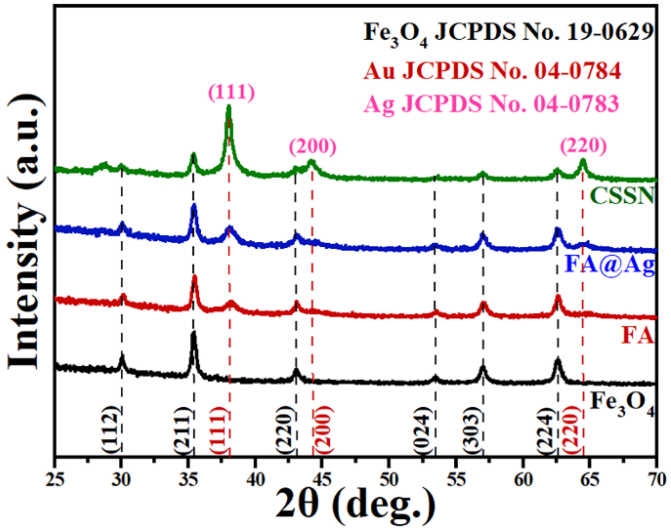

Figure 1. XRD pattern of Fe_3O_4 hollow spheres, FA, FA@Ag, and CSSN NCs.

For researching the magnetic properties of Fe_3O_4 hollow spheres, FA, FA@Ag, and CSSN NCs, their magnetic hysteresis (*M-H*) loops were tested via vibrating sample magnetometer (VSM), as displayed in Figure S2. The *M-H* loops show that Fe_3O_4 hollow spheres, FA, FA@Ag, and CSSN NCs have superparamagnetic property. The saturation magnetization (Ms) values of Fe_3O_4 hollow spheres, FA, FA@Ag, and CSSN NCs were 89.1, 74.5, 63.7, and 53.6 emu·g^{-1}, respectively. It was found that the Ms value gradually reduces with the incremental introduction of noble metal due to the diamagnetism of noble metal nanocrystals [52]. As depicted in the inset of Figure S2, the CSSN NCs can be collected by an external magnet within 50 s even if their Ms value is the lowest among all the materials. The remarkable magnetic response property means that CSSN NCs have great convenience in rapid separation and detection in complex liquid environments.

The morphology, size, and structure of the obtained products were studied by TEM, EDS elemental mapping, and EDS line scanning. As depicted in Figure 2a, the Fe_3O_4 nanocrystals show uniform spherical shapes with size of about 600 nm, and the dark edges and shallow cores of Fe_3O_4 nanocrystals suggest the formation of hollow structures. It can be seen from the TEM image of FA NCs (Figure 2b) that Au seeds (about 20 nm) are densely and uniformly loaded on the surfaces of Fe_3O_4 hollow spheres. Subsequently, the seed-mediated growth technique was used to grow Ag shell on the surfaces of FA NCs. Specifically, Au seeds on Fe_3O_4 hollow spheres were employed as nucleation sites for the formation of Ag shells. As exhibited in the dark-field TEM image of FA@Ag NCs (Figure 2c), with the continuous reduction of Ag^+ on surfaces of FA NCs, Ag shells with subtle roughness formed on the surfaces of FA NCs, and elements of Au and Ag are uniformly distributed on the surfaces of Fe_3O_4 hollow spheres, as shown in the corresponding EDS elemental mapping in Figure 2c. In order to create more hot spots, Au@Ag nanocrystals continued to be assembled on the surfaces of FA@Ag NCs to obtain CSSN NCs by PEI-DTC layers. As presented in Figure 2d, PEI-DTC layers with a thickness of around 15 nm are uniformly coated on the surfaces of FA@Ag NCs. For directly confirming the construction of core–shell–satellite structure in CSSN NCs, we took EDS line scanning profiles (Figure 2f) across CSSN NCs as presented by the orange highlighted line in the dark-field TEM image of Figure 2e. As shown in Figure 2f, it was found that the size of

CSSN NCs increased to around 800 nm due to the presence of Au seeds, Ag shells, and Au@Ag nanocrystals, which is bigger than that of Fe_3O_4 hollow spheres. Moreover, the elements show a symmetrical distribution with the change of detection position. The X-ray intensity of Au and Ag is maximum while Fe and O is minimum in the edge region. By comparison, the relative intensity of Fe and O increases gradually and almost no X-ray intensity of Au and Ag is observed in the direction of the orange arrow. This proves that the Au@Ag nanocrystals are adsorbed firmly on the outermost layer of FA@Ag@PEI-DTC by the affinities between the bidentate ligands with two chelating sulfur groups and Au@Ag nanocrystals [31]. Therefore, the EDS line-scanning results of CSSN NCs are consistent with the conclusions of XRD, TEM, and corresponding EDS mapping, which proves that the formation of CSSN NCs with the core–shell–satellite structure is convincing.

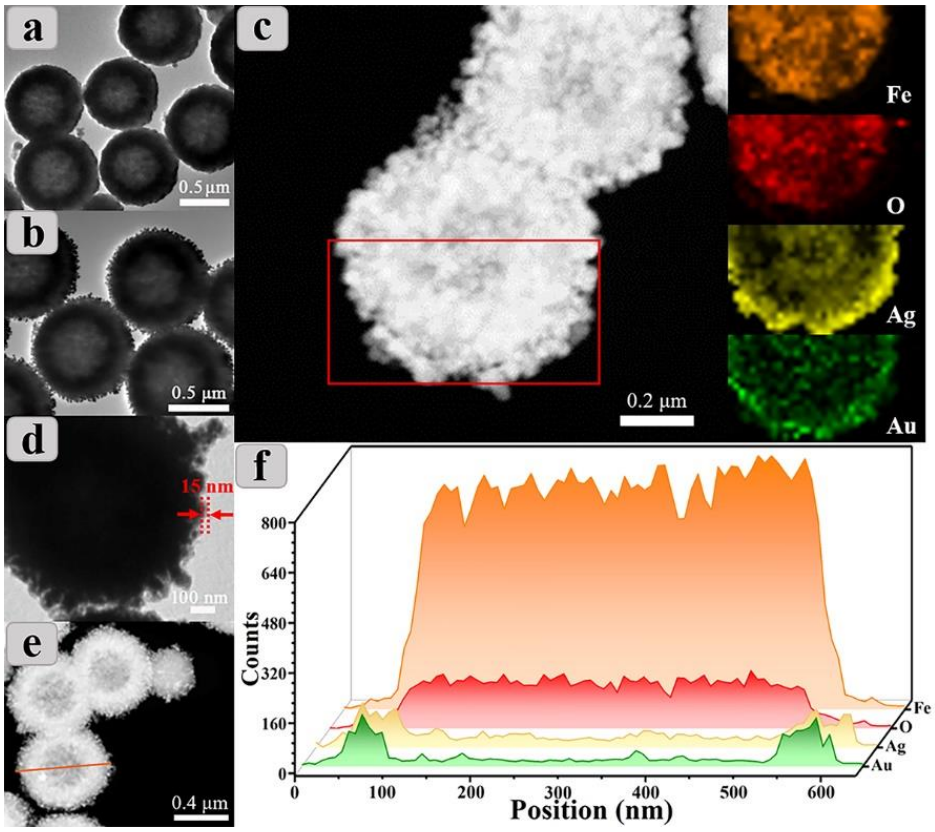

Figure 2. TEM images of Fe_3O_4 hollow spheres (**a**) and FA NCs (**b**). Dark-field TEM images and EDS elemental mapping results (O, Fe, Au and Ag) of FA@Ag NCs (**c**). TEM image of FA@Ag@PEI-DTC NCs (**d**). Dark-field TEM images (**e**) and EDS line scanning spectra of CSSN NCs (**f**).

The valence of elements in CSSN NCs was determined by XPS technology. Full XPS spectra of Fe_3O_4 hollow spheres, FA, FA@Ag, and CSSN NCs are exhibited in Figure S3. Within detection limit of XPS, Fe 2p, O1s, Au 4f, Ag 3d, and C 1s were observed and no impurity was found. High-resolution XPS results of Ag 3d and Au 4f are reflected in Figure 3. Ag 3d spectra in Figure 3a display peaks at 368.2 and 374.2 eV with a spin-orbit splitting of 6 eV for CSSN NCs, which are attributable to characteristics of Ag $3d_{3/2}$ and Ag $3d_{5/2}$ of Ag^0 [53]. As represented in Figure 3b, peaks of CSSN NCs at 84.1 and 87.8 eV with an energy difference of 3.7 eV are attributable to Au $4f_{7/2}$ and Au $4f_{5/2}$ of Au^0 [54,55]. An interesting phenomenon is that the binding energy of Ag 3d as well as Au 4f changes slightly with the incremental introduction of noble metals. The positions of Ag 3d peaks of CSSN NCs are blue-shifted compared with FA@Ag NCs, and the positions of Au 4f peaks are red-shifted compared with FA@Ag and FA NCs. This shift in binding energy may be ascribed to the charge transfer from metallic Au to Ag [56–58].

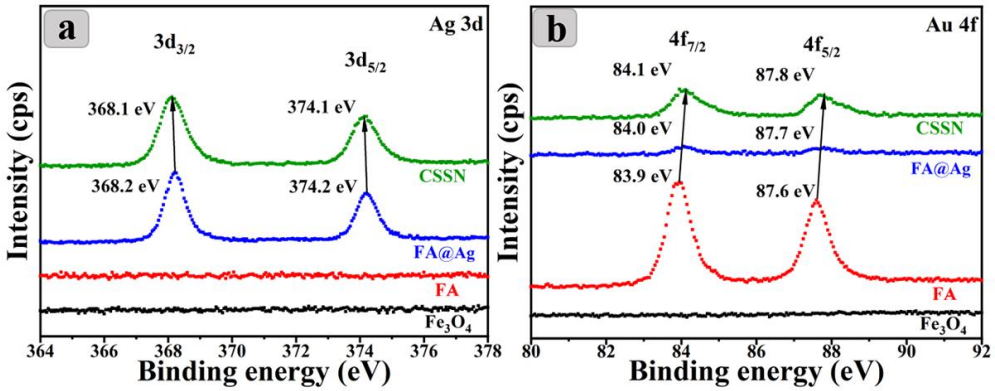

Figure 3. High-resolution XPS spectra of Fe_3O_4 hollow spheres, FA, FA@Ag, and CSSN NCs: Ag 3d (**a**) and Au 4f (**b**).

3.2. Choice of Excitation Source

A widely accepted consensus is that the SERRS method can further improve the sensitivity of Raman scattering spectroscopy, which combines resonance enhancement and SERS [59]. Hence, it is very important to find a suitable excitation source to arouse the SERRS effect. UV–Vis spectra of BPA azo products, FA, FA@Ag, and CSSN NCs were tested to determine a light source with an appropriate wavelength that takes into account the resonance effect of BPA azo products and plasmon resonance effect of CSSN NCs with the laser. As presented in Figure S4, the absorption positions of BPA azo products, FA, FA@Ag, and CSSN NCs are located at 450, 545, 536, and 512 nm, respectively. Because the plasmonic resonance peak of CSSN NCs is closer to the absorption position of BPA azo products compared with FA and FA@Ag NCs, the coupling between BPA azo products and CSSN NCs is considerably easier. Therefore, 514.5 nm laser was selected as the excitation source in this work given that it is more suitable for the coupling absorption.

3.3. SERRS Spectra of BPA Azo Product on FA, FA@Ag, and CSSN NCs

In order to directly evaluate the SERRS performance of various substrates, BPA (10^{-4} M) was chosen as the target molecule and FA, FA@Ag, and CSSN NCs served as SERRS substrates to explore their SERRS-enhancing capabilities, respectively. The detailed band assignments of BPA azo products are exhibited in Table S2 [37,60]. As reflected in Figure 4, with the incremental introduction of noble metals, the SERRS intensity of BPA gradually increases and CSSN NCs exhibit the strongest SERRS sensitivity compared with FA and FA@Ag NCs. The above phenomenon is foreseeable and will be discussed in detail below.

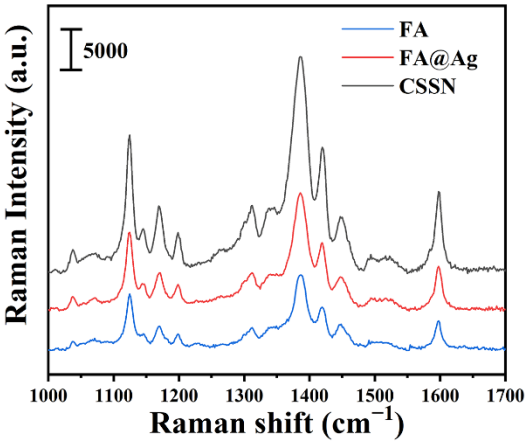

Figure 4. SERRS spectra after azo reaction of BPA azo products (10^{-4} M) on FA, FA@Ag, and CSSN NCs.

3.4. Mechanism of SERRS Enhancement

As mentioned above, the widely accepted theory for SERRS enhancement mechanism is EM mechanism, which derives from LSPR excitation of noble metal nanocrystals [61–63]. Compared with FA NCs, the surfaces of FA@Ag NCs are almost completely covered with Ag shells, which have better LSPR effect than Au, so it is reasonable that SERRS performance of FA@Ag NCs is somewhat better than that of FA NCs. In addition, strong electromagnetic fields will be excited in/between nearby noble metals because of the coupling effect and thus the SERRS signal intensity of target molecule can be significantly enhanced in hot spot regions [64–66]. Consequently, increasing the quantity of hot spots is an effective method to enhance the SERRS activity. To reveal why CSSN NCs have the highest SERRS enhancement, a FDTD theoretical algorithm was employed to visualize the distribution of electromagnetic field. As presented in Figure 5, it can be seen that more hot spots are generated on CSSN NCs. Compared with CSSN NCs, no obvious hot spots are found on the separate FA@Ag NCs (Figure 5a). A reasonable explanation is that the SERRS enhancement of FA@Ag NCs may come from hot spots generated by the aggregation of FA@Ag NCs in an actual detection procedure. As for CSSN NCs, large number of hot spots can also emerge in the region of narrow spacing between two adjacent Au@Ag nanocrystals, as shown in Figure 5b,c. In addition, there are large amounts of hot spots between Ag shells and outermost Au@Ag nanocrystals. It follows that the hot-spots effect is brought into full play through the construction of the core–shell–satellite structure. It also needs to be emphasized here that the introduction of the bimetallic Au@Ag nanocrystals is distinctly important, given that the Au@Ag nanocrystals make full use of excellent SERRS activity of Ag nanocrystals and high stability of Au nanocrystals [67,68]. Therefore, the excellent SERRS performance of CSSN NCs is attributed to a considerable quantity of hot spots generated by the core–shell–satellite structure, as well as excellent SERRS performance of Au@Ag nanocrystals.

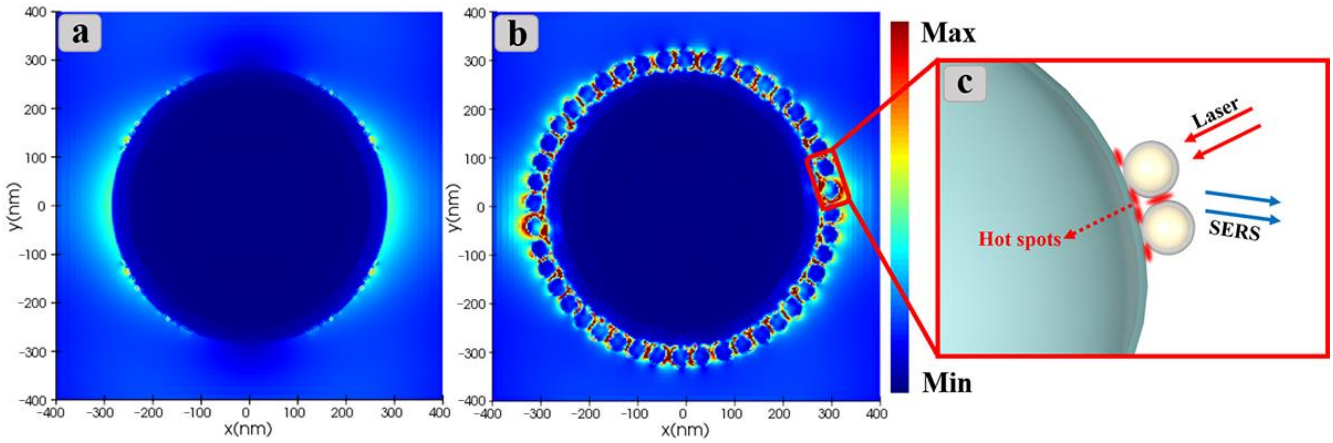

Figure 5. Electric field distribution of FA@Ag (**a**) and CSSN NCs (**b**) obtained by FDTD theoretical algorithm and the diagrammatic sketch of hot spots on CSSN NCs (**c**).

3.5. Quantitative Detection of BPA Azo Products

In order to assess the practicability of CSSN NCs as SERRS substrate for quantitative and sensitive detection of BPA, BPA azo products with different concentration from 10^{-10} to 10^{-4} M were chosen as probe molecules. Sharp and strong characteristic peaks of BPA azo products can be clearly observed from SERRS spectra illustrated in Figure 6a. SERRS intensities of BPA azo products rise monotonously with the increase of concentrations. The limit of detection (LOD) for the detection of BPA is as low as 10^{-10} M (about 0.023 ng/mL), which is well below the safety limit of the European Union (0.6 mg/kg), as well as China (10 ng/mL) [69]. More importantly, compared with the previous reports, our as-prepared CSSN substrate has the highest SERRS enhancement performance (Table 1) [70–75]. Moreover, the relationship between the concentrations of BPA azo products adsorbed on CSSN

NCs and the corresponding SERRS intensities at 1384 cm^{-1} is reflected in Figure 6b. The linear relationship versus the logarithm of the concentrations and correlation coefficient (R^2) is up to 0.96, which further proves that CSSN NCs are high performance SERRS sensors and can realize quantification of BPA down to 10^{-10} M.

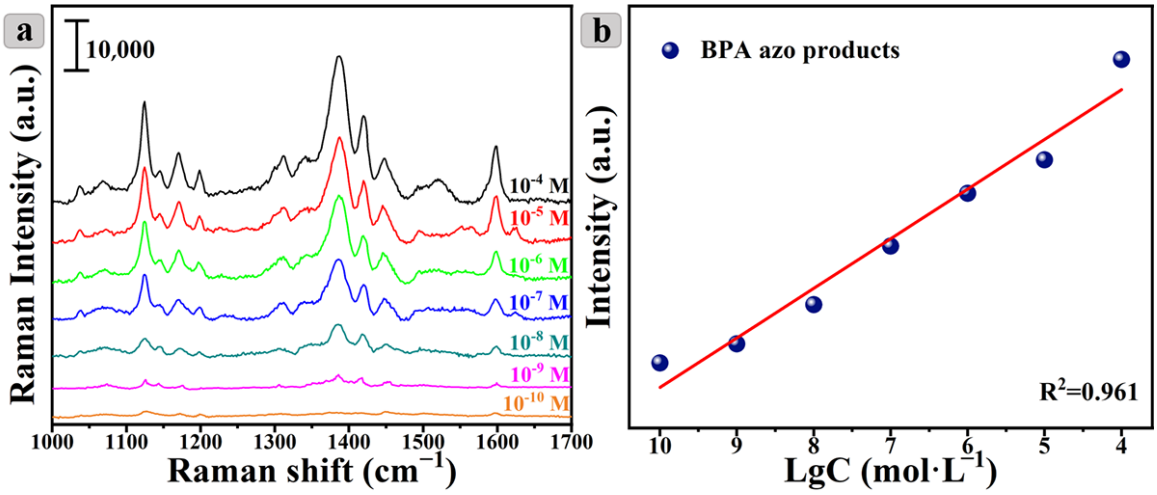

Figure 6. SERRS spectra of BPA azo products (from 10^{-10} to 10^{-4} M) adsorbed on CSSN NCs (**a**). The relationship between the SERRS intensity and concentrations of BPA azo products (**b**).

Table 1. Comparison of the SERS sensitivity of different SERS substrates to BPA.

SERS Substrates	LOD (M)	References
MoS_2/ZnO	10^{-9}	[70]
Au/MBA/PEG/BADGE	3×10^{-9}	[71]
Self-assembled graphitic substrates	10^{-6}	[72]
Ag-thiolated β-cyclodextrin	10^{-7}	[73]
MIPs@Ag NPs	5×10^{-8}	[74]
Ag@MIP	10^{-9}	[75]
CSSN	10^{-10}	this work

4. Conclusions

In conclusion, magnetic core–shell–satellite CSSN NCs for ultra-sensitive SERRS detection of BPA have been successfully developed. The coupling reactions between BPA and Pauly's reagents not only improved the affinity between BPA and substrates, but also amplified the SERRS signals due to the SERRS effect generated by the combination of resonance of BPA azo products and plasma resonance of noble metals. BPA azo products were chosen as target molecules to investigate the effect of incremental introduction of noble metals on SERRS activity. The distribution of electromagnetic field of CSSN NCs was studied through FDTD theoretical algorithm. The results revealed that a considerable number of hot spots were produced on the core–shell–satellite structure. The excellent SERRS activity of CSSN NCs was attributed to abundant hot spots of core–shell–satellite structure as well as outstanding SERRS activity of Au@Ag nanocrystals. BPA azo products were used to evaluate the practicability of CSSN NCs as SERRS substrate. When the concentrations of BPA azo products ranged from 10^{-10} to 10^{-4} M, SERRS intensities followed linear relationship versus the logarithm of the concentrations, and LOD was as low as 10^{-10} M. In addition, the Ms value of superparamagnetic CSSN NCs was 53.6 emu·g^{-1}, which gave CSSN NCs the function of rapid separation and detection in complex liquid environments by an external magnetic field. This study not only provides a novel ultra-sensitive SERRS substrate, but also shows enormous potential for the field of food safety and environmental pollution control.

Supplementary Materials: The following supporting information can be downloaded at: https://www.mdpi.com/article/10.3390/nano12193322/s1, Figure S1: Mössbauer spectrum of Fe_3O_4 hollow spheres; Figure S2: Magnetic hysteresis (*M-H*) loops of Fe_3O_4 hollow spheres, FA, FA@Ag and CSSN NCs (The inset is photograph of CSSN NCs dispersed in deionized water before and after magnet separation); Figure S3: Full XPS spectra of Fe_3O_4 hollow spheres, FA, FA@Ag and CSSN NCs; Figure S4: UV-Vis spectra of BPA azo products, FA, FA@Ag and CSSN NCs; Table S1: Mössbauer spectrum parameters of Fe_3O_4 hollow spheres; Table S2: Band assignments in the SERRS spectra of BPA azo products.

Author Contributions: Investigation, J.H. and T.Z.; Methodology, J.H.; Formal analysis, J.H. and W.Z.; Writing-original draft, J.H.; Conceptualization, M.Z. and Y.L.; Data curation, Z.Z.; Visualization, W.L.; Visualization, N.R.K.; Supervision, H.L. and Y.L.; Funding acquisition, Y.L.; Writing-review & editing; Y.L. All authors have read and agreed to the published version of the manuscript.

Funding: This work was supported by the National Natural Science Foundation of China, China (No. 21676115), Program for the development of Science and Technology of Jilin province, China (No. 20220203021SF, 20200301043RQ and 20200201022JC) and Program for Science and Technology of Education Department of Jilin Province, China (No. JJKH20210611KJ and JJKH20220444KJ).

Data Availability Statement: Not applicable.

Conflicts of Interest: The authors declare no conflict of interest.

References

1. Ismanto, A.; Hadibarata, T.; Kristanti, R.A.; Maslukah, L.; Safinatunnajah, N.; Kusumastuti, W. Endocrine disrupting chemicals (EDCs) in environmental matrices: Occurrence, fate, health impact, physio-chemical and bioremediation technology. *Environ. Pollut.* **2022**, *302*, 119061. [CrossRef] [PubMed]
2. Al Sharabati, M.; Abokwiek, R.; Al-Othman, A.; Tawalbeh, M.; Karaman, C.; Orooji, Y.; Karimi, F. Biodegradable polymers and their nano-composites for the removal of endocrine-disrupting chemicals (EDCs) from wastewater: A review. *Environ. Res.* **2021**, *202*, 111694. [CrossRef] [PubMed]
3. Astrahan, P.; Korzen, L.; Khanin, M.; Sharoni, Y.; Israel, A. Seaweeds fast EDC bioremediation: Supporting evidence of EE2 and BPA degradation by the red seaweed Gracilaria sp., and a proposed model for the remedy of marine-borne phenol pollutants. *Environ. Pollut.* **2021**, *278*, 116853. [CrossRef]
4. Kobroob, A.; Peerapanyasut, W.; Kumfu, S.; Chattipakorn, N.; Wongmekiat, O. Effectiveness of N-Acetylcysteine in the Treatment of Renal Deterioration Caused by Long-Term Exposure to Bisphenol A. *Biomolecules* **2021**, *11*, 655. [CrossRef] [PubMed]
5. Khan, M.R.; Ouladsmane, M.; Alammari, A.M.; Azam, M. Bisphenol A leaches from packaging to fruit juice commercially available in markets. *Food Packag. Shelf* **2021**, *28*, 100678. [CrossRef]
6. Sousa, S.; Maia, M.L.; Delerue-Matos, C.; Calhau, C.; Domingues, V.F. The role of adipose tissue analysis on Environmental Pollutants Biomonitoring in women: The European scenario. *Sci. Total Environ.* **2022**, *806*, 150922. [CrossRef] [PubMed]
7. Din, S.T.U.; Lee, H.; Yang, W. Z-Scheme Heterojunction of 3-Dimensional Hierarchical Bi_3O_4Cl/Bi_5O_7I for a Significant Enhancement in the Photocatalytic Degradation of Organic Pollutants (RhB and BPA). *Nanomaterials* **2022**, *12*, 767. [CrossRef] [PubMed]
8. Wang, X.; Nag, R.; Brunton, N.P.; Siddique, M.A.B.; Harrison, S.M.; Monahan, F.J.; Cummins, E. Human health risk assessment of bisphenol A (BPA) through meat products. *Environ. Res.* **2022**, *213*, 113734. [CrossRef]
9. Makowska, K.; Staniszewska, M.; Bodziach, K.; Calka, J.; Gonkowski, S. Concentrations of bisphenol a (BPA) in fresh pork loin meat under standard stock-farming conditions and after oral exposure—A preliminary study. *Chemosphere* **2022**, *295*, 133816. [CrossRef]
10. Escarda-Castro, E.; Herraez, M.P.; Lombo, M. Effects of bisphenol A exposure during cardiac cell differentiation. *Environ. Pollut.* **2021**, *286*, 117567. [CrossRef]
11. Santhi, V.A.; Hairin, T.; Mustafa, A.M. Simultaneous determination of organochlorine pesticides and bisphenol A in edible marine biota by GC-MS. *Chemosphere* **2012**, *86*, 1066–1071. [CrossRef] [PubMed]
12. Murugananthan, M.; Yoshihara, S.; Rakuma, T.; Shirakashi, T. Mineralization of bisphenol A (BPA) by anodic oxidation with boron-doped diamond (BDD) electrode. *J. Hazard. Mater.* **2008**, *154*, 213–220. [CrossRef] [PubMed]
13. Latif, A.; Maqbool, A.; Sun, K.; Si, Y. Immobilization of Trametes Versicolor laccase on Cu-alginate beads for biocatalytic degradation of bisphenol A in water: Optimized immobilization, degradation and toxicity assessment. *J. Environ.Chem. Eng.* **2022**, *10*, 107089. [CrossRef]
14. Xue, C.S.; Erika, G.; Jiri, H. Surface plasmon resonance biosensor for the ultrasensitive detection of bisphenol A. *Anal. Bioanal. Chem.* **2019**, *411*, 5655–5658. [CrossRef] [PubMed]
15. Jia, M.; Chen, S.; Shi, T.; Li, C.; Wang, Y.; Zhang, H. Competitive plasmonic biomimetic enzyme-linked immunosorbent assay for sensitive detection of bisphenol A. *Food Chem.* **2021**, *344*, 128602. [CrossRef]

16. Dai, J.; Baker, G.L.; Bruening, M.L. Use of Porous Membranes Modified with Polyelectrolyte Multilayers as Substrates for Protein Arrays with Low Nonspecific Adsorption. *Anal. Chem.* **2006**, *78*, 135–140. [CrossRef] [PubMed]
17. Xie, Y.; Ma, L.; Ling, S.; Ouyang, H.; Liang, A.; Jiang, Z. Aptamer-Adjusted Carbon Dot Catalysis-Silver Nanosol SERS Spectrometry for Bisphenol A Detection. *Nanomaterials* **2022**, *12*, 1374. [CrossRef]
18. Simonenko, N.P.; Musaev, A.G.; Simonenko, T.L.; Gorobtsov, P.Y.; Volkov, I.A.; Gulin, A.A.; Simonenko, E.P.; Sevastyanov, V.G.; Kuznetsov, N.T. Hydrothermal Synthesis of Ag Thin Films and Their SERS Application. *Nanomaterials* **2021**, *12*, 136. [CrossRef] [PubMed]
19. Zhu, Z.; Bai, B.; You, O.; Li, Q.; Fan, S. Fano resonance boosted cascaded optical field enhancement in a plasmonic nanoparticle-in-cavity nanoantenna array and its SERS application. *Light Sci. Appl.* **2015**, *4*, e296. [CrossRef]
20. Wu, R.; Jin, Q.; Storey, C.; Collins, J.; Gomard, G.; Lemmer, U.; Canham, L.; Kling, R.; Kaplan, A. Gold nanoplasmonic particles in tunable porous silicon 3D scaffolds for ultra-low concentration detection by SERS. *Nanoscale Horiz.* **2021**, *6*, 781–790. [CrossRef]
21. Morton, S.M.; Silverstein, D.W.; Jensen, L. Theoretical studies of plasmonics using electronic structure methods. *Chem. Rev.* **2011**, *111*, 3962–3994. [CrossRef] [PubMed]
22. Yang, S.; Yao, J.; Quan, Y.; Hu, M.; Su, R.; Gao, M.; Han, D.; Yang, J. Monitoring the charge-transfer process in a Nd-doped semiconductor based on photoluminescence and SERS technology. *Light Sci. Appl.* **2020**, *9*, 117. [CrossRef] [PubMed]
23. Zong, C.; Xu, M.; Xu, L.; Wei, T.; Ma, X.; Zheng, X.; Hu, R.; Ren, B. Surface-Enhanced Raman Spectroscopy for Bioanalysis: Reliability and Challenges. *Chem. Rev.* **2018**, *118*, 4946–4980. [CrossRef] [PubMed]
24. Pandey, P.; Seo, M.K.; Shin, K.H.; Lee, Y.W.; Sohn, J.I. Hierarchically Assembled Plasmonic Metal-Dielectric-Metal Hybrid Nano-Architectures for High-Sensitivity SERS Detection. *Nanomaterials* **2022**, *12*, 401. [CrossRef] [PubMed]
25. Sun, Y.; Zhang, C.; Yuan, Y.; Xu, M.; Yao, J. The moveable "hot spots" effect in an Au nanoparticles-Au plate coupled system. *Nanoscale* **2020**, *12*, 23789–23798. [CrossRef]
26. Shao, Y.; Li, S.; Niu, Y.; Wang, Z.; Zhang, K.; Mei, L.; Hao, Y. Three-Dimensional Dendritic Au-Ag Substrate for On-Site SERS Detection of Trace Molecules in Liquid Phase. *Nanomaterials* **2022**, *12*, 2002. [CrossRef]
27. Baffou, G.; Bordacchini, I.; Baldi, A.; Quidant, R. Simple experimental procedures to distinguish photothermal from hot-carrier processes in plasmonics. *Light Sci. Appl.* **2020**, *9*, 108. [CrossRef]
28. Weber, M.L.; Willets, K.A. Correlated Super-Resolution Optical and Structural Studies of Surface-Enhanced Raman Scattering Hot Spots in Silver Colloid Aggregates. *J. Phys. Chem. Lett.* **2011**, *2*, 1766–1770. [CrossRef]
29. Zhang, Y.; Wang, Z.; Zhang, Q.; Song, Y.; Zhang, B.; Ren, T.; Yang, H.; Wang, F. Polyethyleneimine mediated interaction for highly sensitive, magnetically assisted detection of tetracycline hydrochloride. *Appl. Surf. Sci.* **2020**, *505*, 144543. [CrossRef]
30. Wang, R.; Yan, X.; Ge, B.; Zhou, J.; Wang, M.; Zhang, L.; Jiao, T. Facile Preparation of Self-Assembled Black Phosphorus-Dye Composite Films for Chemical Gas Sensors and Surface-Enhanced Raman Scattering Performances. *ACS Sustain. Chem. Eng.* **2020**, *8*, 4521–4536. [CrossRef]
31. Liu, Y.; Zhang, Y.; Kou, Q.; Wang, D.; Han, D.; Lu, Z.; Chen, Y.; Chen, L.; Wang, Y.; Zhang, Y.; et al. Fe_3O_4/Au binary nanocrystals: Facile synthesis with diverse structure evolution and highly efficient catalytic reduction with cyclability characteristics in 4-nitrophenol. *Powder Technol.* **2018**, *338*, 26–35. [CrossRef]
32. Ji, Y.; Yang, S.; Guo, S.; Song, X.; Ding, B.; Yang, Z. Bimetallic Ag/Au nanoparticles: A low temperature ripening strategy in aqueous solution. *Colloid. Surface. A* **2010**, *372*, 204–209. [CrossRef]
33. Yang, Y.; Liu, J.; Fu, Z.; Qin, D. Galvanic replacement-free deposition of Au on Ag for core-shell nanocubes with enhanced chemical stability and SERS activity. *J. Am. Chem. Soc.* **2014**, *136*, 8153–8156. [CrossRef]
34. Ke, Y.; Chen, B.; Hu, M.; Zhou, N.; Huang, Z.; Meng, G. In-Situ Monitoring the SERS Spectra of para-Aminothiophenol Adsorbed on Plasmon-Tunable Au@Ag Core-Shell Nanostars. *Nanomaterials* **2022**, *12*, 1156. [CrossRef]
35. Svedendahl, M.; Verre, R.; Käll, M. Refractometric biosensing based on optical phase flips in sparse and short-range-ordered nanoplasmonic layers. *Light Sci. Appl.* **2014**, *3*, e220. [CrossRef]
36. Yin, W.; Wu, L.; Ding, F.; Li, Q.; Wang, P.; Li, J.; Lu, Z.; Han, H. Surface-imprinted SiO_2@Ag nanoparticles for the selective detection of BPA using surface enhanced Raman scattering. *Sensor. Actuat. B Chem.* **2018**, *258*, 566–573. [CrossRef]
37. Han, X.; Pienpinijtham, P.; Zhao, B.; Ozaki, Y. Coupling reaction-based ultrasensitive detection of phenolic estrogens using surface-enhanced resonance Raman scattering. *Anal. Chem.* **2011**, *83*, 8582–8588. [CrossRef] [PubMed]
38. Blanco-Covian, L.; Montes-Garcia, V.; Girard, A.; Fernandez-Abedul, M.T.; Perez-Juste, J.; Pastoriza-Santos, I.; Faulds, K.; Graham, D.; Blanco-Lopez, M.C. Au@Ag SERRS tags coupled to a lateral flow immunoassay for the sensitive detection of pneumolysin. *Nanoscale* **2017**, *9*, 2051–2058. [CrossRef]
39. Ishmukhametov, I.; Batasheva, S.; Rozhina, E.; Akhatova, F.; Mingaleeva, R.; Rozhin, A.; Fakhrullin, R. DNA/Magnetic Nanoparticles Composite to Attenuate Glass Surface Nanotopography for Enhanced Mesenchymal Stem Cell Differentiation. *Polymers* **2022**, *14*, 344. [CrossRef]
40. Kou, Y.; Wu, T.; Zheng, H.; Kadasala, N.R.; Yang, S.; Guo, C.; Chen, L.; Liu, Y.; Yang, J. Recyclable magnetic MIP-based SERS sensors for selective, sensitive, and reliable detection of paclobutrazol residues in complex environments. *ACS Sustain. Chem.* **2020**, *8*, 14549–14556. [CrossRef]
41. Dong, S.; Rene, E.R.; Zhao, L.; Xiaoxiu, L.; Ma, W. Design and preparation of functional azo linked polymers for the adsorptive removal of bisphenol A from water: Performance and analysis of the mechanism. *Environ. Res.* **2022**, *206*, 112601. [CrossRef] [PubMed]

42. Jaguey-Hernandez, Y.; Aguilar-Arteaga, K.; Ojeda-Ramirez, D.; Anorve-Morga, J.; Gonzalez-Olivares, L.G.; Castaneda-Ovando, A. Biogenic amines levels in food processing: Efforts for their control in foodstuffs. *Food Res. Int.* **2021**, *144*, 110341. [CrossRef] [PubMed]
43. Tuo, Y.; Liu, G.; Dong, B.; Zhou, J.; Wang, A.; Wang, J.; Jin, R.; Lv, H.; Dou, Z.; Huang, W. Microbial synthesis of Pd/Fe_3O_4, Au/Fe_3O_4 and PdAu/Fe_3O_4 nanocomposites for catalytic reduction of nitroaromatic compounds. *Sci. Rep.* **2015**, *5*, 13515. [CrossRef]
44. Qu, J.; Liu, G.; Wang, Y.; Hong, R. Preparation of Fe_3O_4–chitosan nanoparticles used for hyperthermia. *Adv. Powder Technol.* **2010**, *21*, 461–467. [CrossRef]
45. Pinto, P.S.; Lanza, G.D.; Souza, M.N.; Ardisson, J.D.; Lago, R.M. Surface restructuring of red mud to produce FeOx(OH)y sites and mesopores for the efficient complexation/adsorption of beta-lactam antibiotics. *Environ. Sci. Pollut. R.* **2018**, *25*, 6762–6771. [CrossRef]
46. Liu, Y.; Zhang, Y.; Kou, Q.; Chen, Y.; Han, D.; Wang, D.; Lu, Z.; Chen, L.; Yang, J.; Xing, G. Eco-friendly seeded Fe_3O_4-Ag nanocrystals: A new type of highly efficient and low cost catalyst for methylene blue reduction. *RSC Adv.* **2018**, *8*, 2209–2218. [CrossRef] [PubMed]
47. Chen, Y.; Zhang, Y.; Kou, Q.; Liu, Y.; Han, D.; Wang, D.; Sun, Y.; Zhang, Y.; Wang, Y.; Lu, Z.; et al. Enhanced Catalytic Reduction of 4-Nitrophenol Driven by Fe_3O_4-Au Magnetic Nanocomposite Interface Engineering: From Facile Preparation to Recyclable Application. *Nanomaterials* **2018**, *8*, 353. [CrossRef] [PubMed]
48. Han, D.; Li, B.; Chen, Y.; Wu, T.; Kou, Y.; Xue, X.; Chen, L.; Liu, Y.; Duan, Q. Facile synthesis of Fe_3O_4@Au core-shell nanocomposite as a recyclable magnetic surface enhanced Raman scattering substrate for thiram detection. *Nanotechnology* **2019**, *30*, 465703. [CrossRef] [PubMed]
49. Shen, J.; Zhu, Y.; Yang, X.; Zong, J.; Li, C. Multifunctional Fe_3O_4@Ag/SiO_2/Au core-shell microspheres as a novel SERS-activity label via long-range plasmon coupling. *Langmuir* **2013**, *29*, 690–695. [CrossRef] [PubMed]
50. Kahle, M.; Kleber, M.; Jahn, R. Review of XRD-based quantitative analyses of clay minerals in soils: The suitability of mineral intensity factors. *Geoderma* **2002**, *109*, 191–205. [CrossRef]
51. Hill, R.J.; Foxworthy, A.M.; White, R.J. PEAKS®: A PC-based method for quantitative X-ray diffraction phase analysis of lead-acid battery materials. *J. Power Sources* **1990**, *32*, 315–328. [CrossRef]
52. Zhao, W.; Zhang, D.; Zhou, T.; Huang, J.; Wang, Y.; Li, B.; Chen, L.; Yang, J.; Liu, Y. Aptamer-conjugated magnetic Fe_3O_4@Au core-shell multifunctional nanoprobe: A three-in-one aptasensor for selective capture, sensitive SERS detection and efficient near-infrared light triggered photothermal therapy of Staphylococcus aureus. *Sensor. Actuat. B Chem.* **2022**, *350*, 130879. [CrossRef]
53. Zhang, F.; Li, Y.; Qi, M.; Tang, Z.; Xu, Y. Boosting the activity and stability of Ag-Cu_2O/ZnO nanorods for photocatalytic CO_2 reduction. *Appl. Catal. B Environ.* **2020**, *268*, 118380. [CrossRef]
54. Li, Z.; Zhang, Y.; Zhang, H.; Yi, J. MOF-derived Au-loaded Co_3O_4 porous hollow nanocages for acetone detection. *Sensor. Actuat. B Chem.* **2021**, *344*, 130182. [CrossRef]
55. Kim, S.-H.; Kim, E.-M.; Lee, C.-M.; Kim, D.W.; Lim, S.T.; Sohn, M.-H.; Jeong, H.-J. Synthesis of PEG-Iodine-Capped Gold Nanoparticles and Their Contrast Enhancement in *In Vitro* and *In Vivo* for X-Ray/CT. *J. Nanomater.* **2012**, *2012*, 504026. [CrossRef]
56. Liu, Y.; Kou, Q.; Wang, D.; Chen, L.; Sun, Y.; Lu, Z.; Zhang, Y.; Wang, Y.; Yang, J.; Xing, S.G. Rational synthesis and tailored optical and magnetic characteristics of Fe_3O_4–Au composite nanoparticles. *J. Mater. Sci.* **2017**, *52*, 10163–10174. [CrossRef]
57. Guo, X.; Sun, X.; Guo, Y.; Guo, Y.; Wang, Y.; Wang, L.; Zhan, W. Enhanced catalytic performance for selective oxidation of propene with O_2 over bimetallic Au–Cu/SiO_2 catalysts. *Rare Met.* **2021**, *40*, 1056–1066. [CrossRef]
58. Kruse, N.; Chenakin, S. XPS characterization of Au/TiO_2 catalysts: Binding energy assessment and irradiation effects. *Appl. Catal. A Gen.* **2011**, *391*, 367–376. [CrossRef]
59. Xu, G.; Guo, N.; Zhang, Q.; Wang, T.; Song, P.; Xia, L. A sensitive surface-enhanced resonance Raman scattering sensor with bifunctional negatively charged gold nanoparticles for the determination of Cr(VI). *Sci. Total Environ.* **2022**, *830*, 154598. [CrossRef]
60. Liu, Y.; Chen, Y.; Zhang, Y.; Kou, Q.; Zhang, Y.; Wang, Y.; Chen, L.; Sun, Y.; Zhang, H.; MeeJung, Y. Detection and Identification of Estrogen Based on Surface-Enhanced Resonance Raman Scattering (SERRS). *Molecules* **2018**, *23*, 1330. [CrossRef]
61. Lin, S.; Guan, H.; Liu, Y.; Huang, S.; Li, J.; Hasi, W.; Xu, Y.; Zou, J.; Dong, B. Binary plasmonic assembly films with hotspot-type-dependent surface-enhanced Raman scattering properties. *ACS Appl. Mater. Inter.* **2021**, *13*, 53289–53299. [CrossRef] [PubMed]
62. Wang, Y.; Zhang, M.; Ma, H.; Su, H.; Li, A.; Ruan, W.; Zhao, B. Surface plasmon resonance from gallium-doped zinc oxide nanoparticles and their electromagnetic enhancement contribution to surface-enhanced Raman scattering. *ACS Appl. Mater. Inter.* **2021**, *13*, 35038–35045. [CrossRef] [PubMed]
63. Dias, E.J.C.; Yu, R.; Garcia de Abajo, F.J. Thermal manipulation of plasmons in atomically thin films. *Light Sci. Appl.* **2020**, *9*, 87. [CrossRef]
64. Li, J.; Zhang, Y.; Ding, S.; Panneerselvam, R.; Tian, Z. Core-shell nanoparticle-enhanced Raman spectroscopy. *Chem. Rev.* **2017**, *117*, 5002–5069. [CrossRef] [PubMed]
65. Yin, B.; Ho, W.K.H.; Zhang, Q.; Li, C.; Huang, Y.; Yan, J.; Yang, H.; Hao, J.; Wong, S.H.D.; Yang, M. Magnetic-Responsive Surface-Enhanced Raman Scattering Platform with Tunable Hot Spot for Ultrasensitive Virus Nucleic Acid Detection. *ACS Appl. Mater. Inter.* **2022**, *14*, 4714–4724. [CrossRef] [PubMed]

66. Zhang, Q.; Zhang, Y.; Chen, H.; Zhang, L.; Li, P.; Xiao, H.; Wu, W. One-dimensional nanohybrids based on cellulose nanocrystals and their SERS performance. *Carbohyd. Polym.* **2022**, *284*, 119140. [CrossRef] [PubMed]
67. Zhang, J.; Wu, C.; Yuan, R.; Huang, J.A.; Yang, X. Gap controlled self-assembly Au@Ag@Au NPs for SERS assay of thiram. *Food Chem.* **2022**, *390*, 133164. [CrossRef]
68. Li, X.; Lin, X.; Fang, G.; Dong, H.; Li, J.; Cong, S.; Wang, L.; Yang, S. Interfacial layer-by-layer self-assembly of PS nanospheres and Au@Ag nanorods for fabrication of broadband and sensitive SERS substrates. *J. Colloid Interf. Sci.* **2022**, *620*, 388–398. [CrossRef]
69. Huang, L.; Wang, X. Rapid and sensitive detection of Bisphenol A in water by LF-NMR based on magnetic relaxation switch sensor. *Microchem. J.* **2021**, *163*, 105911. [CrossRef]
70. Quan, Y.; Yao, J.; Yang, S.; Chen, L.; Li, J.; Liu, Y.; Lang, J.; Shen, H.; Wang, Y.; Wang, Y.; et al. ZnO nanoparticles on MoS_2 microflowers for ultrasensitive SERS detection of bisphenol A. *Microchim. Acta* **2019**, *186*, 593. [CrossRef]
71. Marks, H.L.; Pishko, M.V.; Jackson, G.W.; Coté, G.L. Rational Design of a Bisphenol A Aptamer Selective Surface-Enhanced Raman Scattering Nanoprobe. *Anal. Chem.* **2014**, *86*, 11614–11619. [CrossRef] [PubMed]
72. Lin, P.; Hsieh, C.; Hsieh, S. Rapid and Sensitive SERS Detection of Bisphenol A Using Self-assembled Graphitic Substrates. *Sci. Rep.* **2017**, *7*, 16698. [CrossRef] [PubMed]
73. Roschi, E.; Gellini, C.; Ricci, M.; Sanchez-Cortes, S.; Focardi, C.; Neri, B.; Otero, J.C.; López-Tocón, I.; Smulevich, G.; Becucci, M. Surface-Enhanced Raman Spectroscopy for Bisphenols Detection: Toward a Better Understanding of the Analyte–Nanosystem Interactions. *Nanomaterials* **2021**, *11*, 881. [CrossRef]
74. Wang, Z.; Yan, R.; Liao, S.; Miao, Y.; Zhang, B.; Wang, F.; Yang, H. In situ reduced silver nanoparticles embedded molecularly imprinted reusable sensor for selective and sensitive SERS detection of Bisphenol A. *Appl. Surf. Sci.* **2018**, *457*, 323–331. [CrossRef]
75. Ren, X.; Cheshari, E.C.; Qi, J.; Li, X. Silver microspheres coated with a molecularly imprinted polymer as a SERS substrate for sensitive detection of bisphenol A. *Microchim. Acta* **2018**, *185*, 242. [CrossRef] [PubMed]